Supporting Information

Lithium-selective "OR-gate" enables fast-kinetics and ultra-stable Li-rich cathodes for polymer-based solid-state batteries

Qin Wang[a], Yiming Zhang[a], Meng Yao[a,] *, Kang Li[c], Lv Xu[a], Haitao Zhang[b], Xiaopeng Wang[a,] *, Yun Zhang[a,] *

a College of Materials Science and Engineering, Sichuan University, Chengdu 610064, P.R. China

b Beijing Key Laboratory of Ionic Liquids Clean Process, Institute of Process Engineering, Chinese Academy of Sciences, Beijing 100190, P.R. China

c School of Materials Science and Engineering, Dongguan University of Technology, Dongguan 523808, P.R. China

e-mail: yaomeng@scu.edu.cn; wangxiaopeng0620@163.com; y_zhang@scu.edu.cn

Keywords: OR gate; surface modifications; layered oxides; solid-state batteries; lithium-ion batteries

This PDF file includes:

Supplementary Text

Fig. S1 to S36

References

Synthesis of materials

The powder samples of LRLO ($Li_{1.2}Mn_{0.6}Ni_{0.2}O_2$) were prepared through a co-precipitation process followed by high-temperature sintering. Initially, $NiSO_4 \cdot 6H_2O$ and $MnSO_4 \cdot H_2O$ were mixed in deionized water at a specific molar ratio (3:1) and then combined with 4M NaOH solution and added to 2M Na_2SO_4 solution. The resulting precursor was created by continuously stirring in a N_2 environment at a reaction temperature of 60°C, using $NH_3 \cdot H_2O$ as a complexing agent. After the filtration and drying process, the obtained precursor was combined with Li_2CO_3 and sintered in an air tube furnace at 500°C for 5 hours and 900°C for 12 hours to yield the LRLO material.

The modified materials were prepared through a hydrothermal method followed by high-temperature sintering. To achieve LRLO materials coated with layered tetrahedral octahedral tetrahedral structures, SiO_2, $Mg(OH)_2$, and LiF were added to a deionized aqueous solution containing 1 g of LRLO in a molar ratio of 4:3:1.[1] The resulting mixture underwent a hydrothermal reaction at 120°C for 8 hours to get intermediate, followed by sintering at high temperatures of 300°C, 500°C, and 800°C in Al_2O_3 crucibles for 1 hour to obtain LRLO-CS, LRLO-OG, and LRLO-CS-800 samples, respectively. Additionally, pure phase coating materials were prepared using the same method without the addition of LRLO.

Characterization of materials

In this study, a comprehensive examination of the material morphology was conducted using various analytical techniques. Optical microscopy (YUESCOPE) and scanning electron microscopy (SEM, ZEISS Gemini 300) were employed to study the material surface features. Additionally, crystal structure investigations were carried out using a FEI Talos-F200S transmission electron microscope (TEM). For qualitative and quantitative analysis of the elemental composition in specific regions, an X-ray energy dispersion spectrometer (EDS) was utilized. In order to test the reaction temperature of the material, Differential Scanning Calorimetry (DSC, NETZSCH TG 209 F1) testing was conducted. Crystal structure determination was accomplished through powder X-ray diffraction (XRD, HY DX-2700BH) and neutron powder diffraction (NPD), with Rietveld refinement analysis performed using the GSAS/EXPGUI program[2]. Raman spectra were obtained using a Thermo DXRMicro Laser Raman spectrometer with a 532 nm excitation laser source. Electron paramagnetic resonance (EPR) measurement was conducted to provide detailed insight into the crystal structure by a Bruker

EMXplus X-band EPR spectrometer with a modulation frequency of 9.86 GHz. Moreover, X-ray photoelectron spectroscopy (XPS) was performed using a Thermo ESCALAB 250XI with an Ar^+ gun, and the surface electrical properties were evaluated using a Zeta potential analyzer (Malvern Zetasizer Nano ZS90). The composition of the material was tested using inductively coupled plasma (ICP, Agilent 5110 OES) and X-ray fluorescence spectrometer (XRF, Rigaku ZSX Primus III+) testing. In order to test the surface charge state of the material, the zeta potential (Malvern Zetasizer Nano ZS90) and dielectric constant (Novocontrol concept 80) of the material were tested. The neutron total scattering data were collected at the Multi-Physics Instrument beamline at room temperature of the China Spallation Neutron Source (CSNS).

Electrochemical measurements

The LRLO cathode electrode was made by mixing active material, acetylene black, and adhesive (polyvinylidene fluoride, PVDF) in a mass ratio of 80:15:5. Then, diluted the resulting slurry in N-methyl-2-pyrrolidone (NMP) and covered it on aluminum foil. Dried the electrodes in a vacuum oven at 120°C for 12 hours. The CR-2032 coin battery (Canrd Technology Co. Ltd) was then assembled in an argon-filled glove box, with the LRLO electrode serving as cathode, lithium foil as the counter electrode, and porous polypropylene film (Calgard 2500) or polyacrylonitrile (PAN) as the separator. All electrochemical tests, including cycling, rate, GITT, and EIS, were performed at 25°C. The pouch cell comprised an LRLO positive electrode, a lithium negative electrode, and a Calgard 2500 separator. After injecting the electrolyte in an argon-filled glove box, the pouch cells were sealed.

Finite-Element Simulation (FEM) simulations

The electric field was predicted with a 2D Nernst-Planck formulation accounting for diffusion and migration in the bulk. The modeling domain, geometrical dimensions, and major boundary conditions are shown in Fig. 5. The governing equations were given as:

$$\nabla^2\varphi = -F\sum z_i\, C_i$$

$$\frac{\partial C_i}{\partial t} = \nabla\cdot\left[D_i\nabla C_i + \frac{D_i C_i}{RT} z_i \nabla\varphi\right]$$

where F, R and T are the Faraday constant, ideal gas constant and temperature, D_i is the

diffusion coefficient. Electroneutrality was assumed throughout the whole domains. In the experiment, the OG fillers. The corresponding boundary conditions on the electrode side and the electrolyte side are specified as 0 V, the length is 500 nm, and the overall diffusion distance is 400 nm. Firstly, considering the situation without the OG fillers, a model with square (50 nm × 50 nm) and initial structure is established to obtain the electric field distribution in different structure. Then, consider that with the OG fillers effect, and then consider the electric field distribution in different deposition states. The model the processed electrochemistry model was imported into the finite element software COMSOL® (Stockholm, Sweden), where the material properties were defined and the relevant problems were calculated and analyzed. To solve the discretized transport and electrode deformation kinematics equations, the Parallel Direct Sparse Solver (PARDISO) was employed. Time stepping was handled using 2nd order backward Euler differentiation.

Ab Initio Molecular Dynamics (AIMD) Simulations

Ab initio molecular dynamics (AIMD) simulations were performed to investigate potential chemical reaction of PAN molecule adsorbed on LRLO (100) and OG (001) surfaces. Firstly, PAN molecules, bulk OG and LRLO unit cell were fully optimized using DMol3 module in Materials Studio (MS) 2020. The exchange correlation potential was described using the generalized gradient approximation (GGA)[3] added in the form of the Perdew-BurkeErnzerhoff (PBE) functional.[4] The double-numeric quality basis sets with polarization functions was used. The iterative tolerances for energy change, force, displacements and self-consistent field (SCF) were 1×10^{-5} Ha, 0.002 Ha $Å^{-1}$, 0.005 Å and 1×10^{-6} a.u., respectively. After structure optimization, we bult LRLO (100) and OG (001) supercell structure. Then, Adsorption Locator Tools[5] in MS were used to place PAN on energy favorable sites of LRLO (100) and OG (001) surface followed by further geometry optimization with bottom layer atom fixing. Here, the Grimme method[6] was applied for DFT dispersion correction. There exists one vacuum layer larger than 15 Å along *c* direction, perpendicular to the surface. Finally, AIMD simulations in DMol3 module under NVT (T = 298 K) ensemble were performed to investigate chemical reaction of PAN on LRLO (100) and OG (001) surfaces. The time step was 1 femtosecond and total running time was 600 femtoseconds.

Density Functional Theory (DFT) Calculations

The diffusion energy barriers of Li^+ on OG (002) surface and in LRLO were respectively evaluated based on density functional theory (DFT). All DFT calculations were carried out using DMol3 module in Materials Studio (MS) 2020. Here, the generalized gradient approximation (GGA) with Perdew–Burke–Ernzerhof (PBE) exchange-correlation functional was employed. The double-numeric quality basis sets with polarization functions were used. The iterative tolerances for energy change, force and displacements were 1×10^{-5} Ha, 0.002 Ha $Å^{-1}$ and 0.005 Å, respectively. After structure optimization, the Adsorption Locator Tools in MS were used to place Li^+ on OG (002) surface and in LRLO, respectively. Then each structure was freely optimized by DMol3 module serving as initial state (IS) and final state (FS) structure, respectively. Here, the bottom layer atoms were fixed. Finally, the complete LST/QST method in DMol3 module was adopted to conduct transition state (TS) search and obtain diffusion energy barriers.

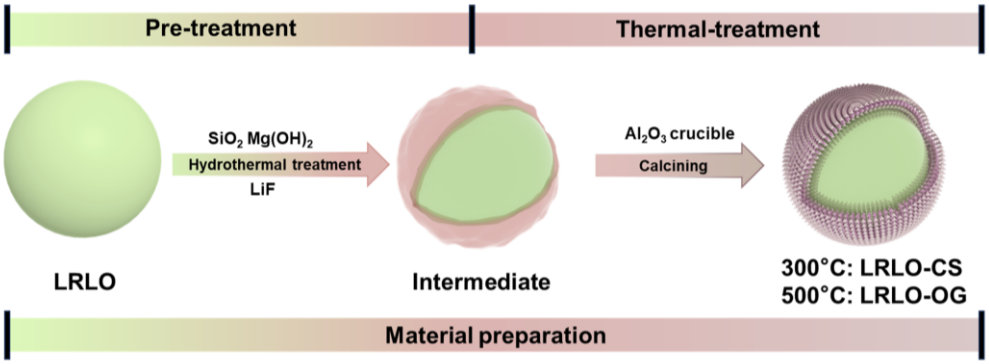

Fig. S1. Schematic diagram of material synthesis process.

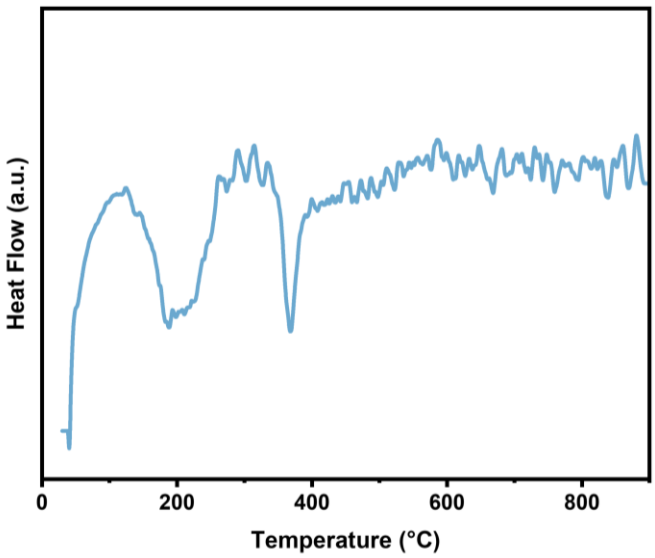

Fig. S2. DSC curves of intermediate.

Differential scanning calorimetry (DSC, Fig. S2) is used to analyze the temperature range of possible reactions that may occur during intermediate sintering process. According to the fluctuation of the heat flow curve, the intermediates are sintered at 300 and 500°C to yield LRLO-CS (contrast sample) and LRLO-OG, respectively. Additionally, CS and OG structures are separately synthesized after sintering at 300 and 500°C without the addition of LRLO.

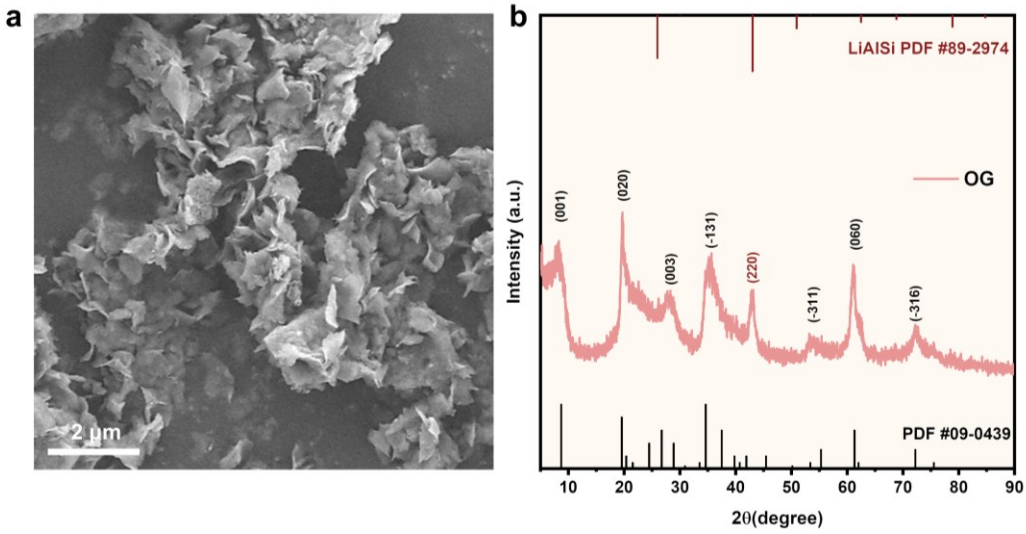

Fig. S3. (a) SEM images of OG. (b) XRD patterns of OG.

The results of the scanning electron microscope (SEM) display a clear sheet-like structure with a uniform element distribution in OG (Fig. S3a). Furthermore, the results of the OG XRD test correspond to a layered structure (PDF#09-0439, Fig. S3b).

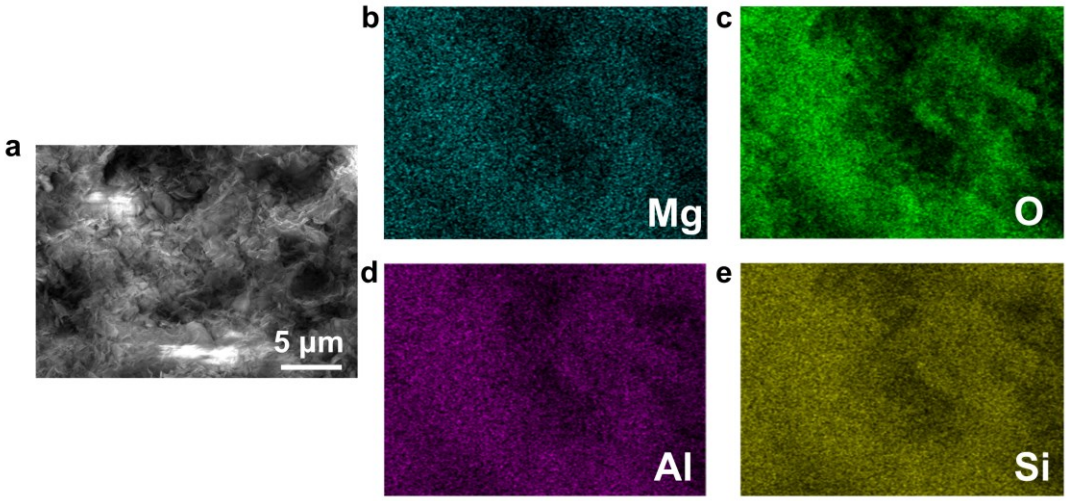

Fig. S4. EDS elements mapping of OG.

As shown in Fig. S4, Al, Mg, and Si are uniformly dispersed on the surface of LRLO-OG. The presence of Al in the sample material lattice is attributed to the use of Al_2O_3 crucibles during the sintering process. Incorporation of Al into the material lattice is expected to enhance the stability of the crystal structure.[7]

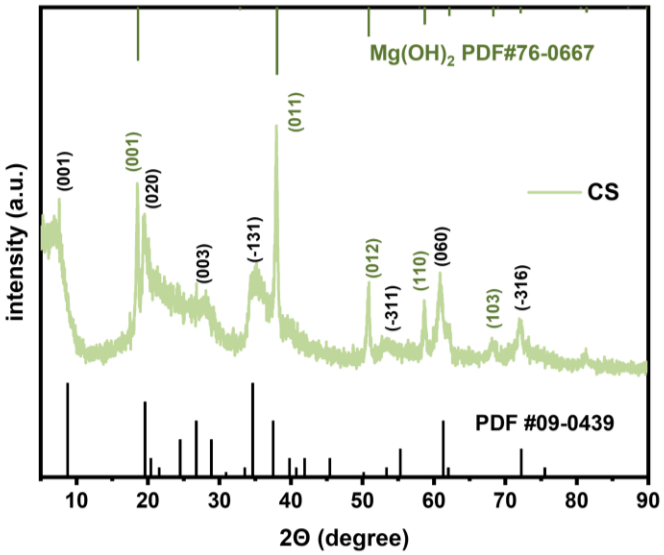

Fig. S5. XRD patterns of CS.

Clear peaks of $Mg(OH)_2$ appear in the XRD spectrum, indicating that the crystal growth of the layered structure is incomplete at lower sintering temperatures.

Table S1 The constituent of OG

Element	Li	Si	Mg	F	O	Al
molar ratio	0.18	2	1	0.24	4.97	1.7%

The proportional formula of OG, $Li_{0.18}Si_2MgF_{0.24}O_{4.97}$, is further determined by inductively coupled plasma and X-ray fluorescence spectrometer tests (Table S1), indicating the successful synthesis of layered OG structure.

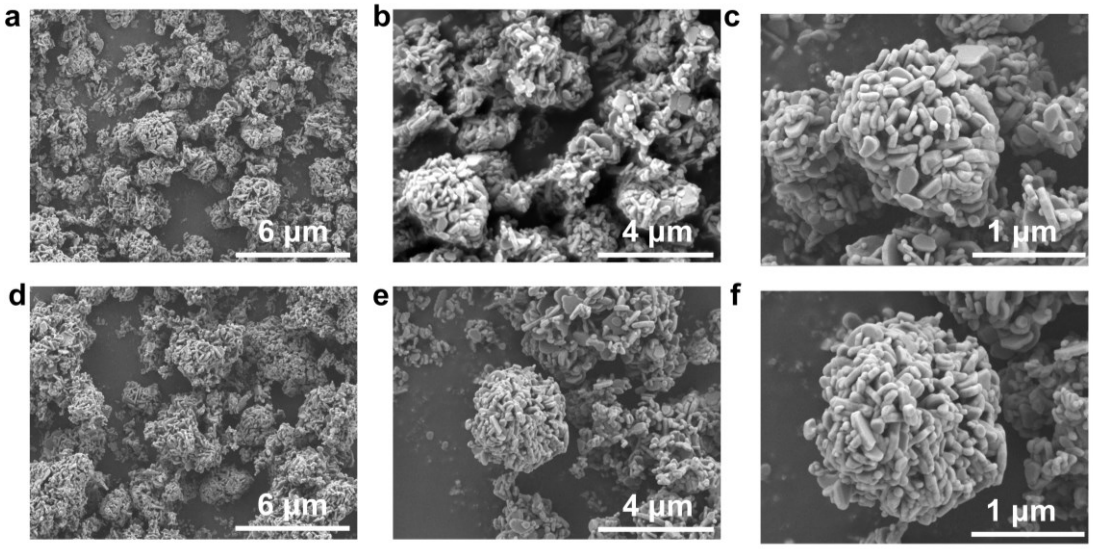

Fig. S6. SEM images of (a-c) LRLO and (d-e) LRLO-OG.

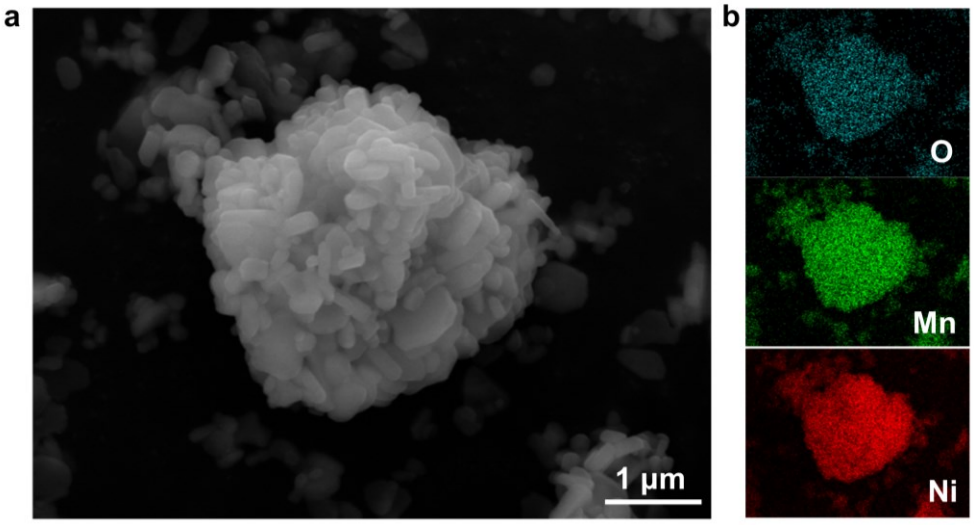

Fig. S7. EDS elements mapping of LRLO.

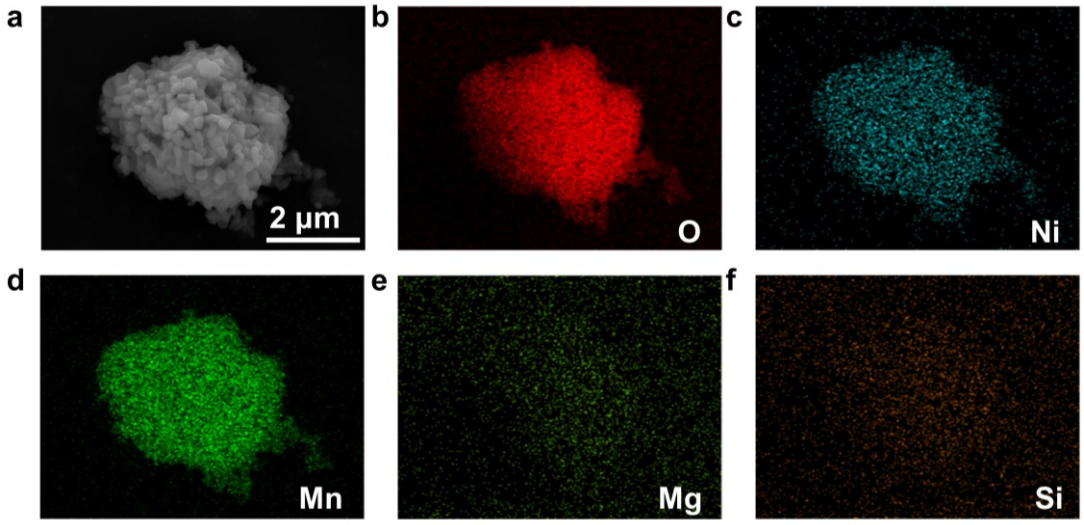

Fig. S8. EDS elements mapping of LRLO-OG.

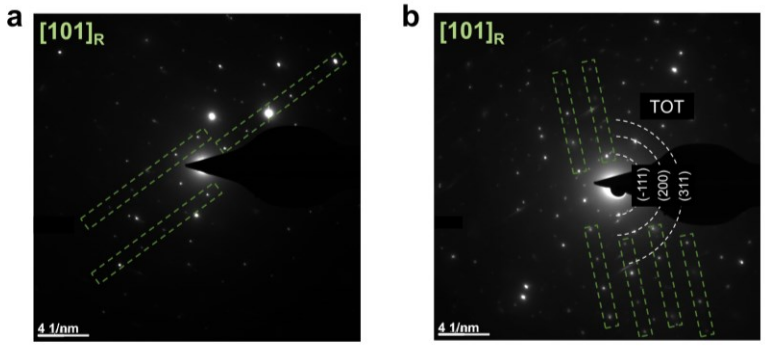

Fig. S9. SAED patterns of (a) LRLO and (b) LRLO-OG.

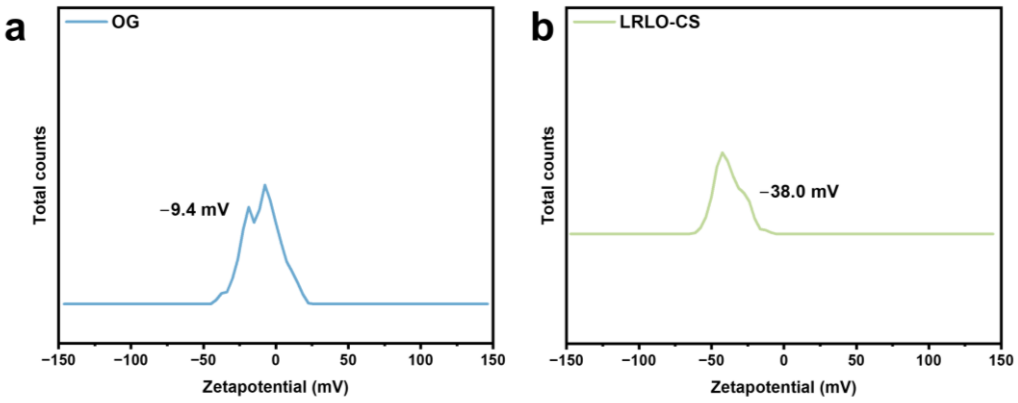

Fig. S10. zeta potential curves of OG and LRLO-CS.

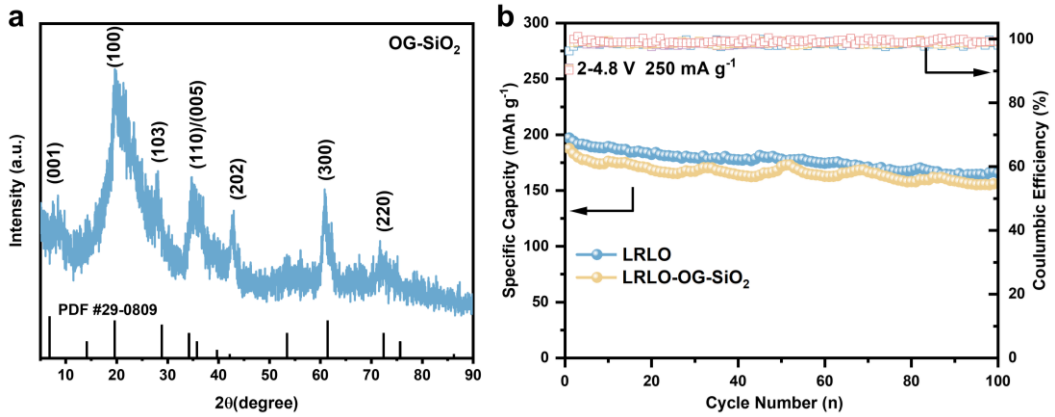

Fig. S11. (a) XRD patterns of OG-SiO_2. (b) Cycling performance of LRLO and LRLO-OG-SiO_2.

When an Al_2O_3 crucible is employed for synthesizing the coating layer material，as shown in Fig. S4, Al, Mg, and Si are uniformly dispersed on the surface of OG. The presence of Al in the lattice of the sample material is ascribed to the utilization of Al_2O_3 crucibles during the sintering process. The incorporation of Al into the material lattice is anticipated to enhance the stability of the crystal structure. More importantly, the low-valence Ni in LRLO enter the sites of Al, leading to an increase in the electronegativity of LRLO-OG and thereby facilitating the diffusion of Li^+. In order to investigate the impact of Al entering the crystal structure of the crucible during sintering on the coating layer, SiO_2 crucibles were employed to sinter at 500°C to obtain LRLO-OG-SiO_2. LRLO-OG-SiO_2 has poorer cycle stability and discharge capacity than LRLO, hence sintering in a SiO_2 crucible will not result in a stable coating.

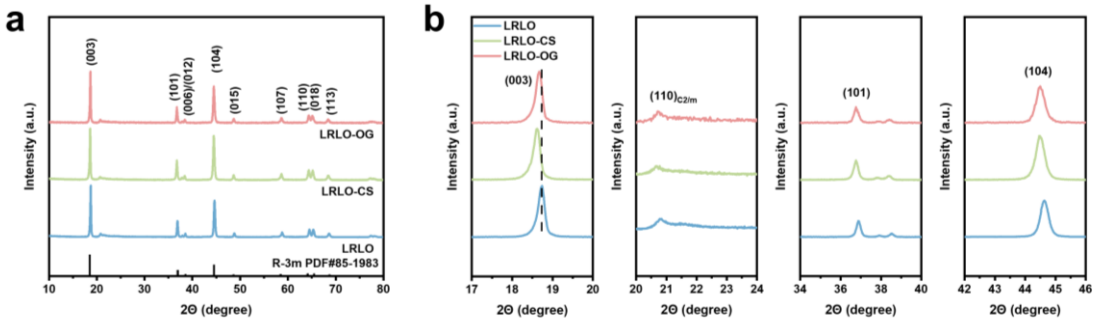

Fig. S12. (a) XRD patterns of LRLO, LRLO-CS and LRLO-OG, (b) Partial amplification of XRD patterns.

The left shift of the (003) peak diffraction angle in LRLO-CS and LRLO-OG, signifying c-axis increase, is due to other elements entering LRLO during modification. This alters lithium-oxygen bonding and oxygen layer repulsion. XPS (Fig. S16) reveals more Mn^{3+} and Ni^{2+} in LRLO-OG. As shown in Fig. S17, the EPR signal in LRLO-CS and LRLO-OG implies Ni^{2+}-Ni^{2+} structures. Higher valance elements from the coating enter LRLO, modifying valence states and crystal structure. What's more, low-valence Ni in LRLO replace Al^{3+} in the coating, making the coated material more negatively charged (Fig. S10). This confirms lattice penetration by coating elements and consequent c-axis increase.

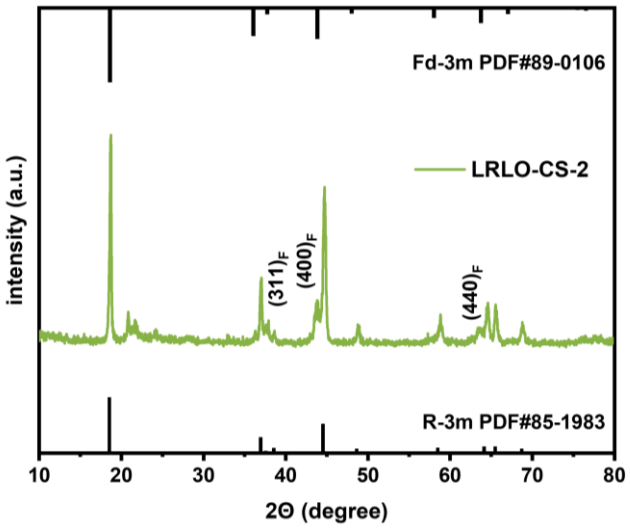

Fig. S13. XRD patterns of LRLO-CS-2.

After doubling the dosage of experiment reagent of LRLO-CS, LRLO-CS-2 are obtained. The XRD results of LRLO-CS-2 clearly depict a spinel structure, suggesting that the impact of the coating layer on the material structure is influenced by the sintering temperature, leading to an increased formation of spinel structures at lower sinter temperature.

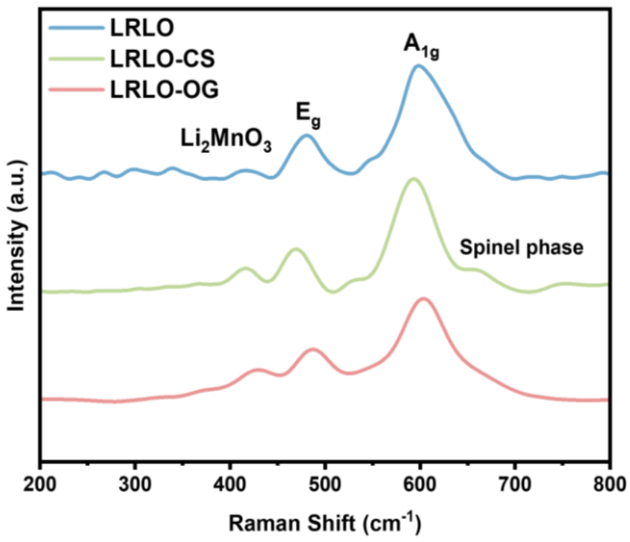

Fig. S14. Raman spectra of LRLO, LRLO-CS and LRLO-OG.

The Raman spectrum of The LRLO-CS demonstrates a distinct peak at a higher Raman shift of 655 cm^{-1}, signifying the formation of a spinel structure.[8] This suggests that the impact of the coating layer on the material structure is influenced by the sintering temperature. The incomplete growth coating at low temperature leads to a structural transformation of LRLO into a spinel structure.

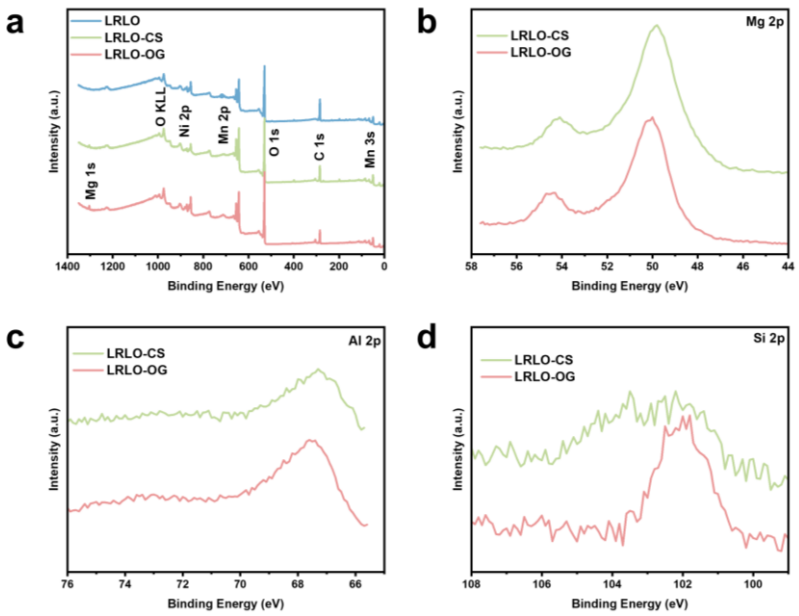

Fig. S15. (a) Wide survey of XPS spectra. XPS spectra of (b) Mg 2p, (c) Al 2p and (d) Si 2p of LRLO-CS and LRLO-OG.

The 2p peaks in the XPS spectrum confirm the presence of Mg, Al, and Si in LRLO-CS and LRLO-OG.

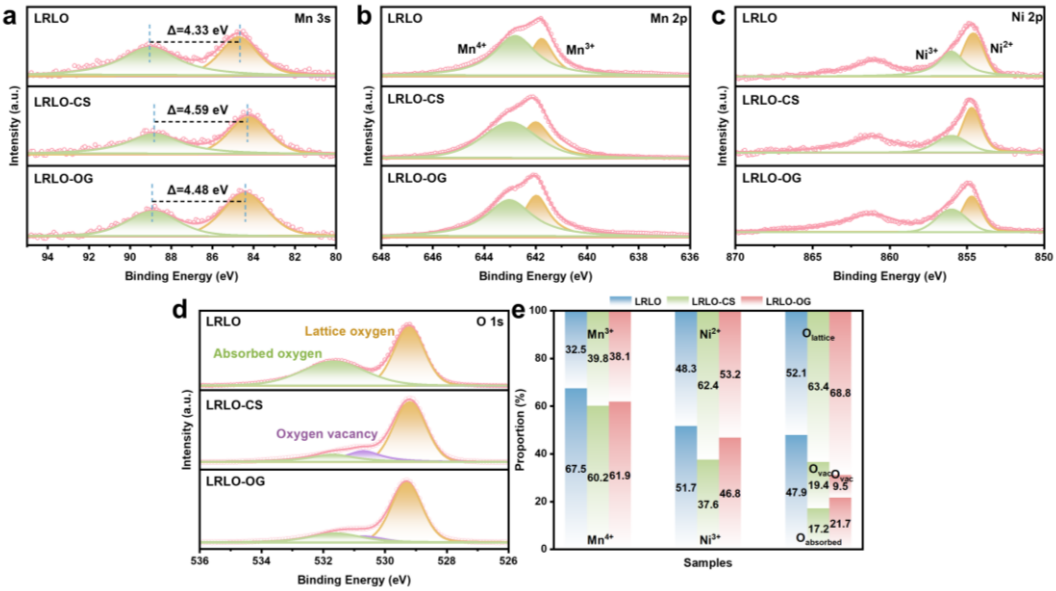

Fig. S16. XPS spectra of (a) Mn 3s, (b) Mn 2p, (c) Ni 2p and (d) O 1s and (e) element proportion of LRLO, LRLO-CS and LRLO-OG.

To investigate the impact of coating on the surface composition of materials, X-ray photoelectron spectroscopy (XPS) is performed, and the results are presented in Fig. S16. As shown in Fig. S16a, the splitting energies of Mn 3s are 4.33 eV, 4.59 eV and

4.48 eV for the LRLO, LRLO-CS and LRLO-OG, respectively. The greater the splitting energy, the smaller the average valence state of Mn.[9] Thus, the valence state of Mn is the highest in LRLO and the lowest in LRLO-CS, owing to the existence of spinel structures with Mn^{3+} in LRLO-CS. The ratio of trivalent and tetravalent Mn obtained from XPS spectra of Mn 2p (Fig. S16b) is shown in Fig. S16e. This is further confirmed the increased proportion of Mn^{3+} in LRLO-CS and LRLO-OG, signifying a decrease in the average valence state of Mn in the after modification materials. The Ni 2p spectrum (Fig. S16c) indicates a higher proportion of Ni^{2+} due to the incorporation of higher valence state elements (Si) into the LRLO crystal for charge balance, leading to a lower Ni valence state. The presence of oxygen vacancies in LRLO-CS and LRLO-OG (Fig. S16d) is advantageous for reducing irreversible oxygen emissions during electrochemical reactions. The unstable absorbed oxygen peak around 531.6 eV that may be originated from the oxidation of C-contained compounds[10], has significantly decreased. The decrease in unstable absorbed oxygen from 47.9% in LRLO to 17.2% in LRLO-CS and 21.7% in LRLO-OG (Fig. S16e) suggests a more stable crystal structure in the modified materials.

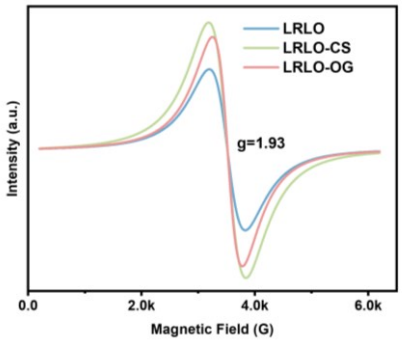

Fig. S17. EPR results of LRLO, LRLO-CS and LRLO-OG.

The strongest EPR signal at g factor 1.93 in LRLO-CS is due to the presence of numerous Ni^{2+}-Ni^{2+} structures with a 180° interaction angle in the material[11], consistent with the XPS results.

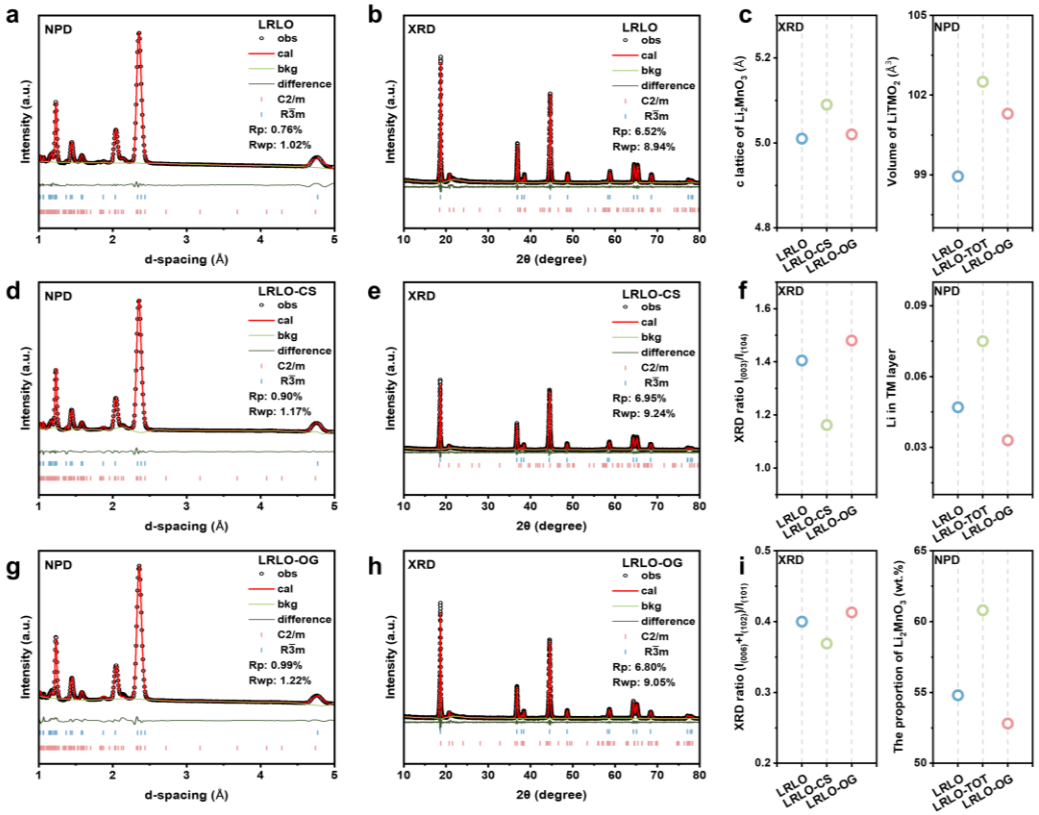

Fig. S18. Testing of Crystal Structure by XRD and NPD. NPD and XRD patterns of (a-b) LRLO, (d-e) LRLO-CS and (g-h) LRLO-OG. Variation of (c) c lattice and volume, (f) the ratio of $I_{(003)}/I_{(104)}$ and Li in TM layer and (i) the ratio of $(I_{(006)}+I_{(102)})/I_{(101)}$ and the proportion of Li2MnO3 in materials calculate by the refinement of XRD and NPD patterns.

To further investigate the impact of modification on crystal structure, neutron powder diffraction (NPD) and XRD data are utilized for Rietveld refinement, as shown in Fig. S18. The resulting changes in the c-axis of Li_2MnO_3 and the volume of $LiTMO_2$ are visually depicted in Fig. S18c. Analysis of the lattice parameters reveals that the c-axis and volume expansion in LRLO-CS and LRLO-OG is pronounced compared to LRLO, especially in LRLO-CS. The expansion observed is correlated with the incorporation of high-valence elements into the lattice, which results in a decrease in the TM valence state and longer TM-O bonds, as indicated by XPS test results[12, 13]. This expansion, while beneficial for ion deintercalation, has the potential to destabilize the crystal structure if it becomes excessive. The interplay between Li/Ni mixing significantly influences the electrochemical performance of LRLO by impeding the diffusion of Li^+. The I_1 ($I_{(003)}/I_{(104)}$) ratio is indicative of the relative abundance of Li^+/Ni^{2+} anti-site defects in the sample, with a higher ratio indicating fewer anti-site defects and greater inter-layer order. As illustrated in Fig. S18f, the Li/Ni mixing of LRLO-CS is the lowest due to the presence of more Ni^{2+} with a radius close to that of Li^+, consistent with previous research results[13]. In addition, the refinement results of

NPD also indicate that there is more Li in the TM layer of LRLO-CS. Conversely, both LRLO and LRLO-OG , characterized by I_1 ratios above 1.4 and lower Li content in the TM layer, demonstrate minimal cation mixing within the layered structure[14]. What's more, the I_2 ($(I_{(006)}+I_{(102)})/I_{(101)}$) ratio and the proportion of Li_2MnO_3 are employed to assess the intra-layer ordering of the sample, with a lower I_2 ratio and higher Li_2MnO_3 riato suggesting the material has more honeycomb-like structures in the transition metal layer[15]. As depicted in Fig. S18i, LRLO-CS contains more honeycomb-like structures, suggesting greater involvement of oxygen in the electrochemical reaction through Li-O-Li structures in the honeycomb-like structure. However, excessive honeycomb-like structure may compromise structural stability. In contrast, the reduction of honeycomb-like structure in LRLO-OG is advantageous for inhibiting oxygen release.

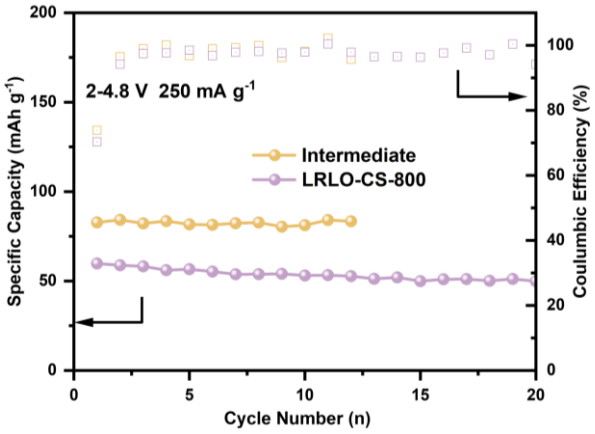

Fig. S19. Cycling performance of unsintered intermediate and sinter under 800°C for 1 hour LRLO-CS-800.

The intermediate and LRLO-CS-800 samples are prepared through the process of sintering and without sintering under 800°C, respectively. The resulting discharge capacities of the intermediate and LRLO-CS-800 samples are remarkably low, measuring only 82.7 and 59.8 mAh g^{-1}. This low capacity can be attributed to the presence of an unstable TOT coating layer on the surface of the intermediate sample. Furthermore, the application of high sintering temperatures caused a significant influx of ions from the coating layers into the LRLO crystal structure, thereby compromising the integrity of the crystal lattice of LRLO-CS-800. Consequently, the discharge capacity of LRLO-CS-800 is reduced as a result of this structural damage.

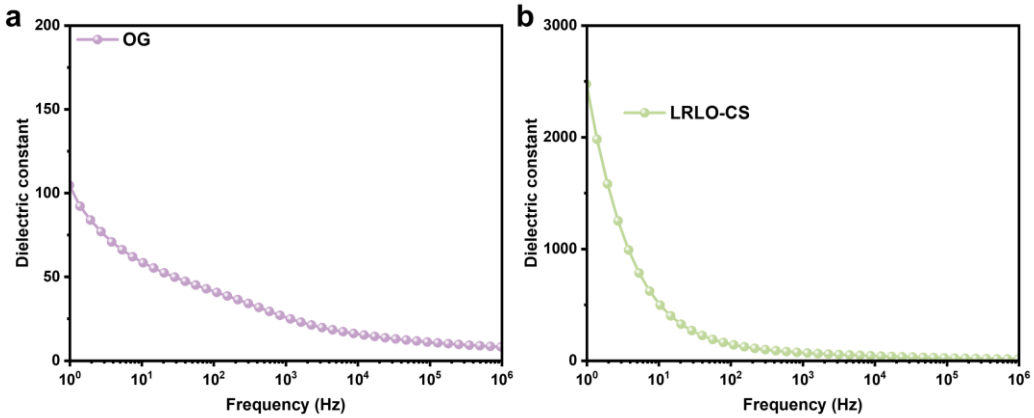

Fig. S20. Dielectric constant of OG and (b) LRLO-CS

The dielectric constant of the coated material is considerably higher than that of the coating layer itself. This is consistent with the zeta potential test results. Further indicating the diffusion of ions between the coating layer and the bulk material, resulting in a significant change in the state of charge of the materials.

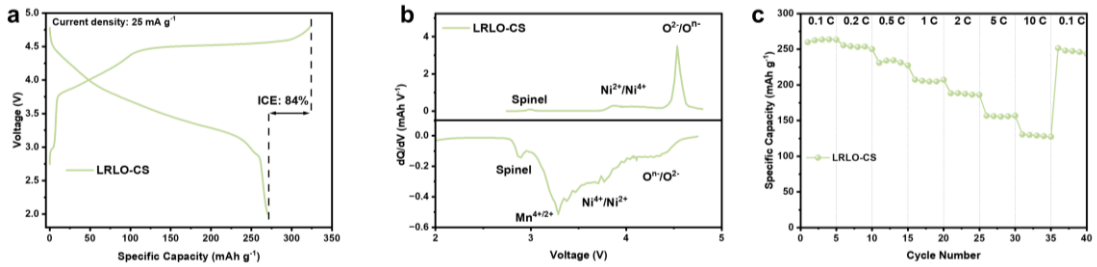

Fig. S21. (a) Initial Charge/discharge curves, (b) Initial dQ/dV curves and (c) rate capability of LRLO-CS at 0.1 C.

The discharge capacity of LRLO-CS (Fig. S21a) reaches 269 mAh g^{-1}. This aligns with previous XRD and NPD test results indicating a greater involvement of Li-O-Li structures in electrochemical reactions in LRLO-CS, thus benefiting capacity enhancement.

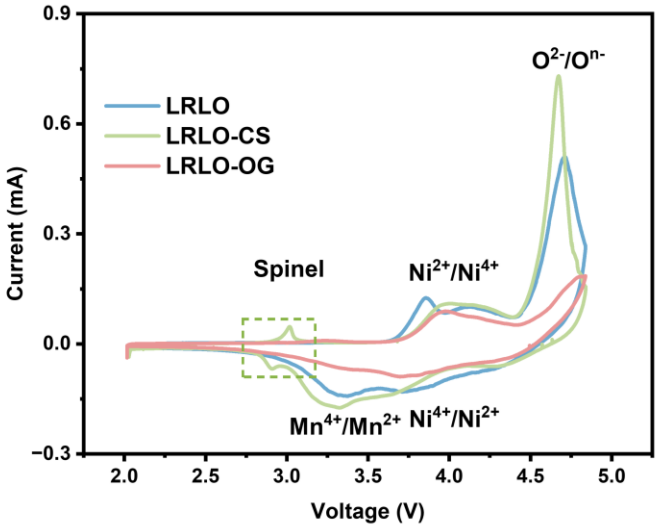

Fig. S22. The first cyclic voltammetry of LRLO, LRLO-CS and LRLO-OG at the scan rate of 0.1 mV s^{-1}.

According to the studies in Fig. S22, it can be seen that the coating material (CS) sintered at low temperatures exhibits stronger oxygen redox reactions. The electrochemical performance of LRLO-CS changes with enhanced oxygen redox peak at 4.6 V. XRD (Fig. S5 and Fig. S13) shows incomplete reactions and much $Mg(OH)_2$ in CS at low temperature, affecting LRLO crystal structure and forming spinel structure. The modifying surface reconstruction path to form spinel phase can improve charge transfer kinetics and alter oxygen redox capacity. XPS (Fig. S16) verifies the change of oxygen state in LRLO-CS. Rietveld refinement of XRD and NPD tests (Fig. S18) defect variations in materials before and after coating. LRLO-CS has higher Li/Ni mixing and more honeycomb-like structures in TM layer, which serves as the foundation for the enhanced oxygen activity.

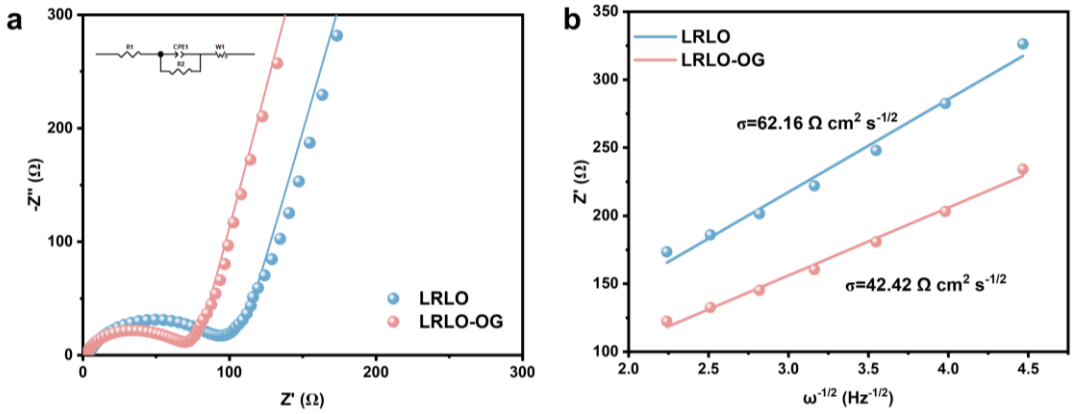

Fig. S23. (a) Nyquist plots and fitting line. (b) Warburg relation of Nyquist plots at pristine state.

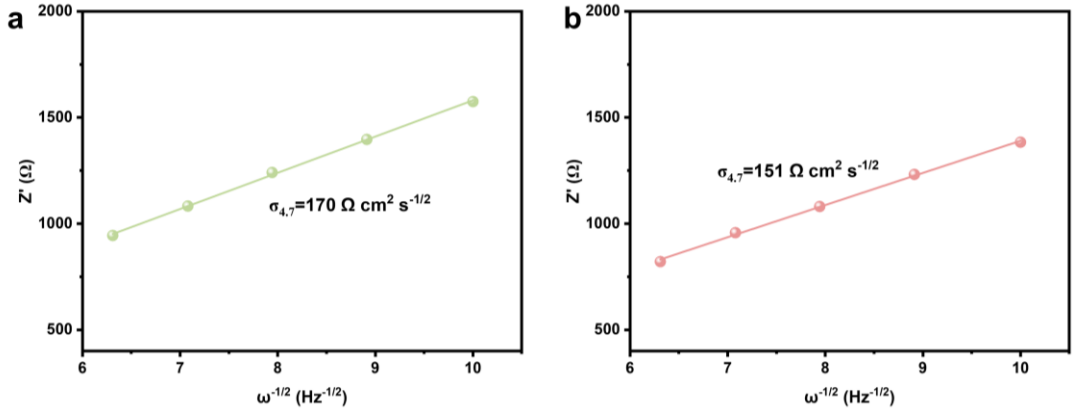

Fig. S24. Warburg relation of Nyquist plots of (a) LRLO and (b) LRLO-OG under a charge voltage of 4.6 V.

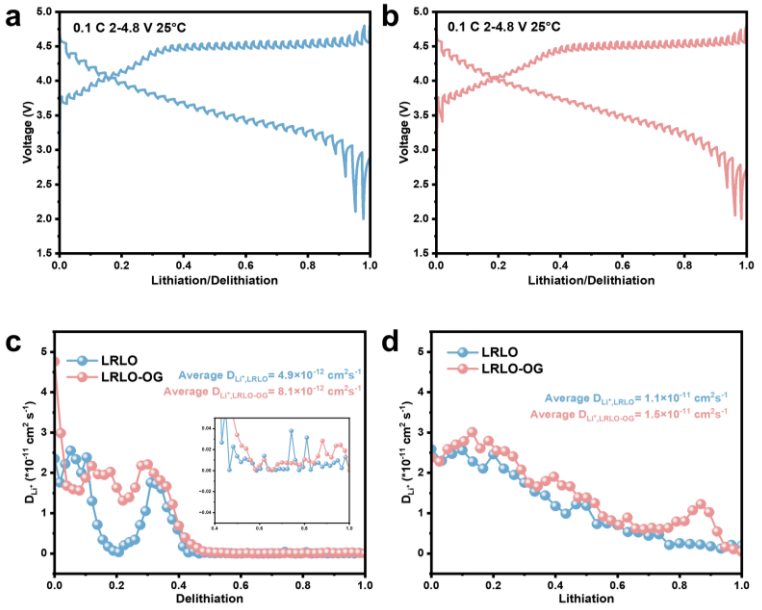

Fig. S25. GITT curves of (a) LRLO and (b) LRLO-OG at 0.1 C; Li^+ diffusion coefficient during (c) charging process and (d) discharging process.

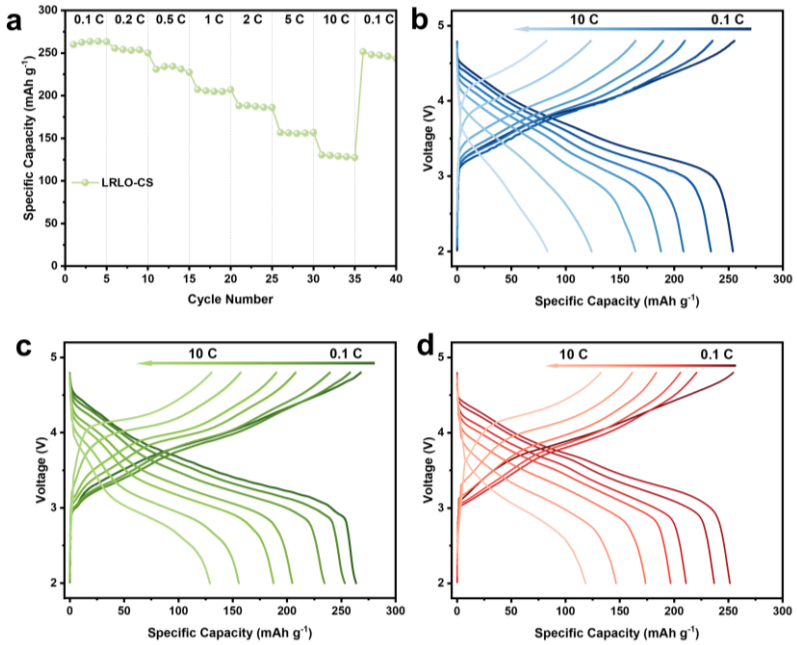

Fig. S26. (a) Rate capability of LRLO-CS. Voltage-capacity curves of (b) LRLO, (c) LRLO-CS and (d) LRLO-OG at different current density.

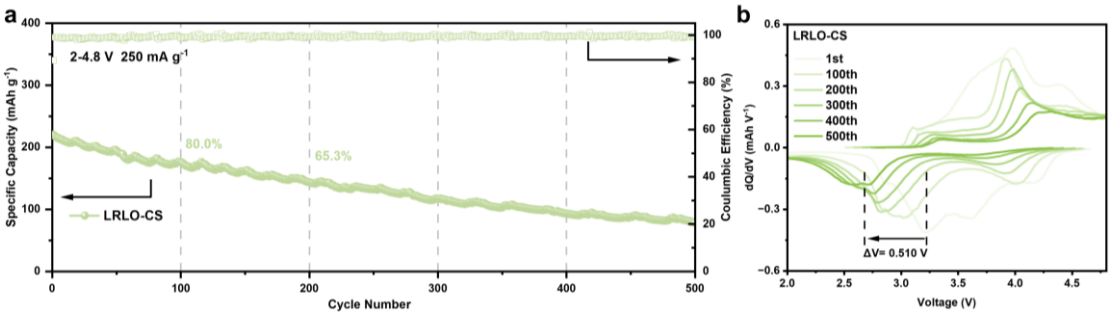

Fig. S27. (a) cycling performance of LRLO-CS. (b) The corresponding dQ/dV curves of cycling performance of LRLO-CS.

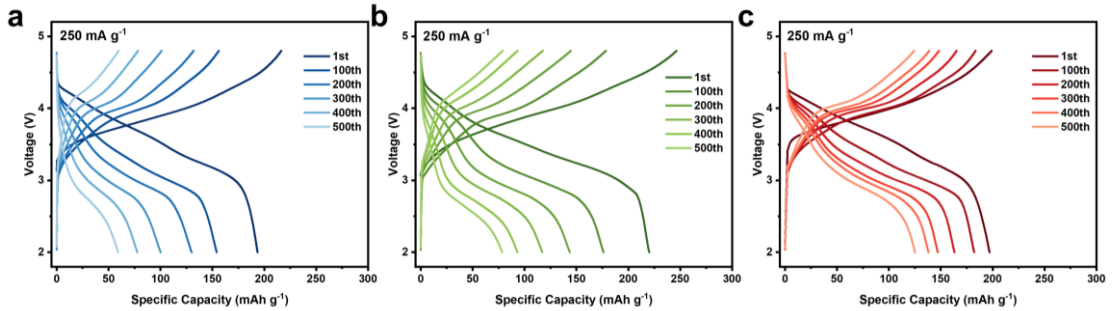

Fig. S28. Voltage-capacity curves of (b) LRLO, (c) LRLO-CS and (d) LRLO-OG after different cycles at a current density of 1 C.

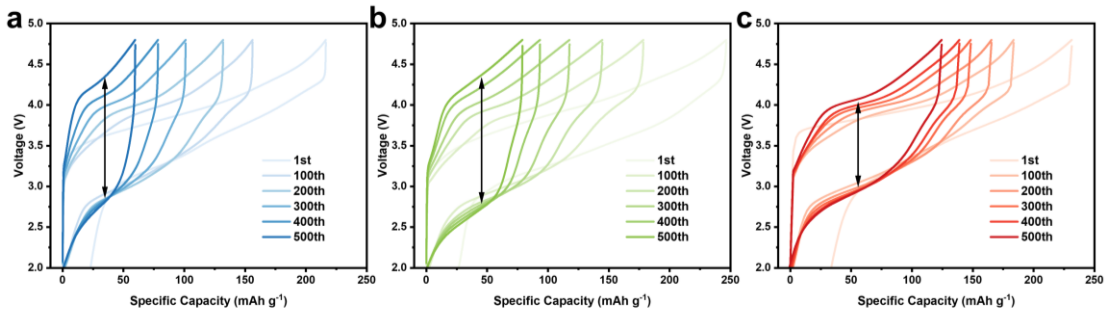

Fig. S29. Voltage hysteresis curves of (a) LRLO, (b) LRLO-CS and (c) LRLO-OG after different cycles at a current density of 1 C.

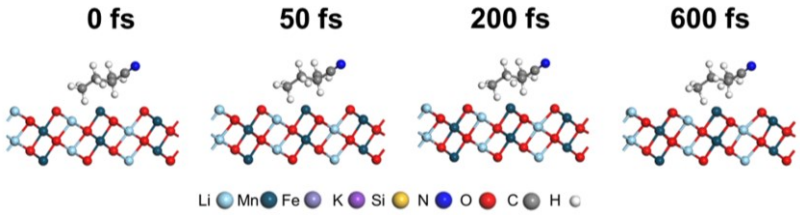

Fig. S30. Obtaining the structure changes of SPE on LRLO Surface from AIMD Simulation.

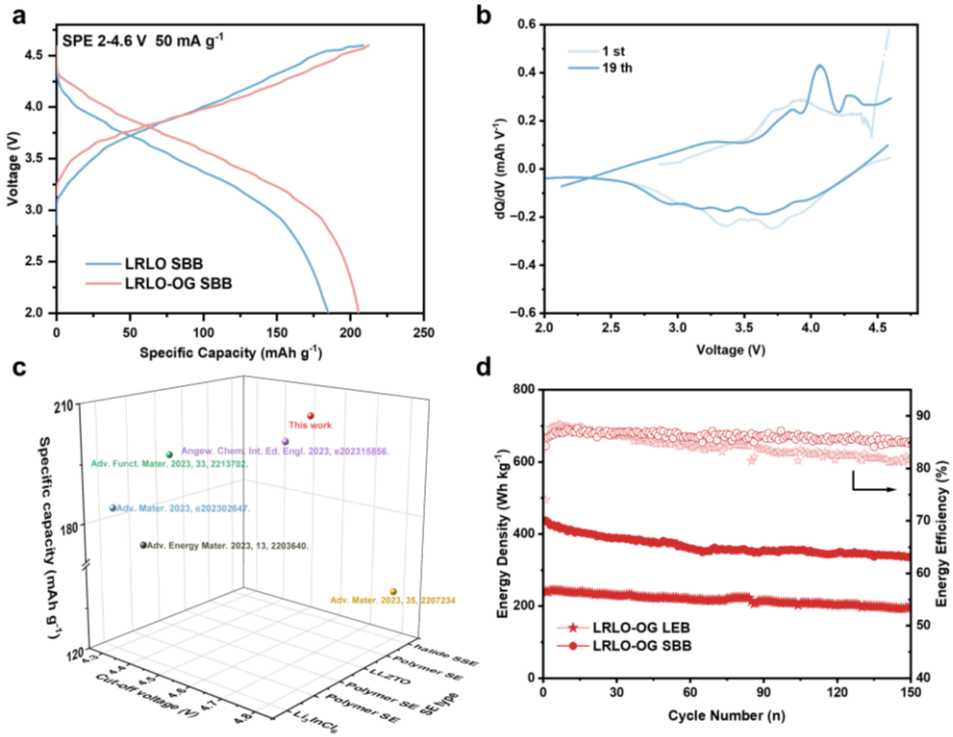

Fig. S31. (a) First charge/discharge curves of LRLO and LRLO-OG in SSB. (b) the corresponding dQ/dV curves of cycling performance of LRLO in SSB. (c) Comparison of electrochemical performance of LRLO-OG and the modified materials in other references in SSBs at o.2 C.[16-20] (d) Energy density during cycling at 0.2 C (LEB is the abbreviation of liquid electrolyte battery).

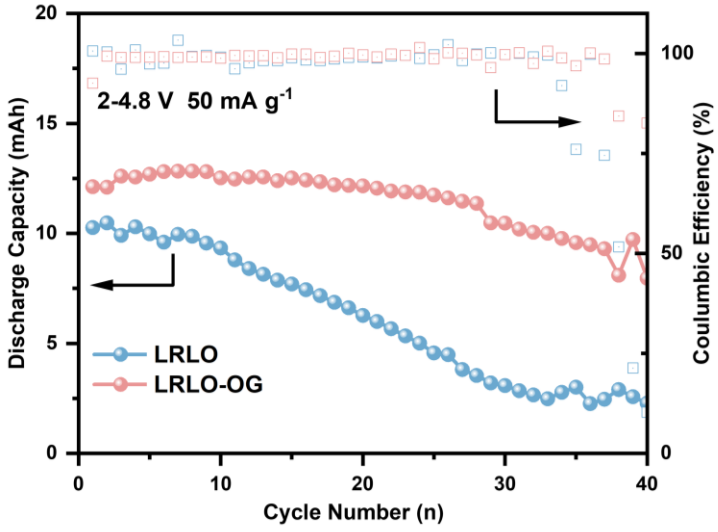

Fig. S32. Pouch cell cycling performance of LRLO and LRLO-OG.

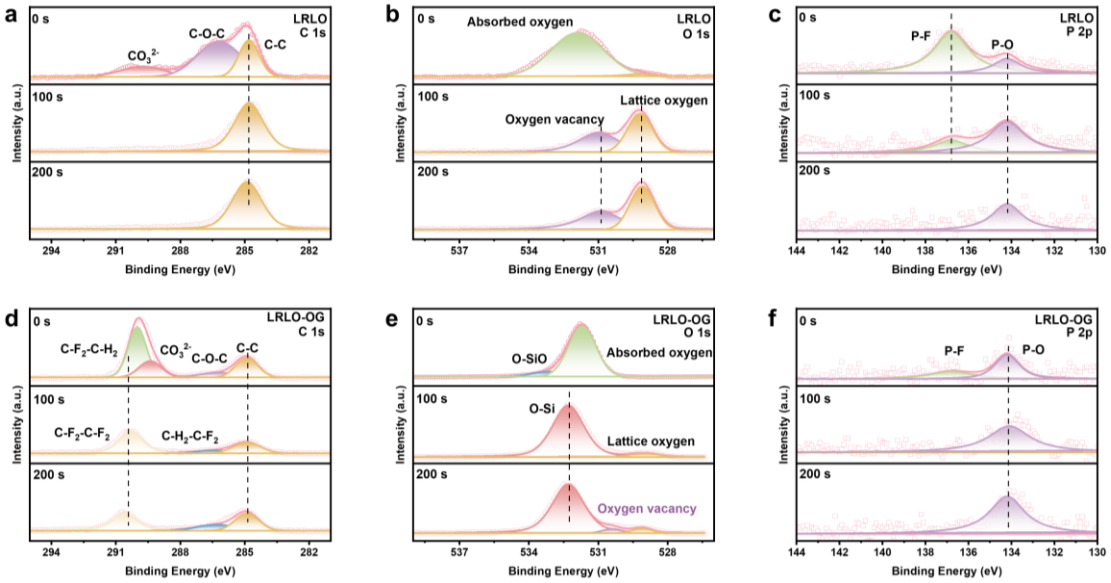

Fig. S33. (a-c) XPS spectra of (a) C 1s, (b) O 1s and (c) P 2p of LRLO after 20th electrochemical cycles and etching for different times. (d-f) XPS spectra of (d) C 1s, (e) O 1s and (f) P 2p of LRLO-OG after 20th electrochemical cycles and etching for different times.

XPS is employed for the examination of the surface composition evolution of electrode material after the electrochemical cycle. As depicted in Fig. S33a, after etching for 100 s and 200 s, the disappearance of peaks for C-O-C and CO_3^{2-}[21] of LRLO indicates that these peaks are attributed to the electrolyte decomposition and the resultant formation of a carbonate surface.[18, 22] Conversely, a reduction intensity in the peak of the C-O-C bond is shown in Fig. S33d, suggesting the effective suppression of interface side reactions in LRLO-OG. Additionally, the appearance of C-F peaks at binding energies of 286.4, 290.0, and 290.4 eV[23, 24] is attributed to the incorporation of LiF during the coating layer synthesis process. When comparing the peak of O 1s spectra in LRLO (Fig. S33b) and LRLO-OG (Fig. S33e), a clear Si-O bonding peak appeared at 532.3 eV in LRLO-OG after etching, which is also a signal of the presence of the coating layer. Comparing the P 2p spectra, it is found that in LRLO-OG (Fig. S33c), the P-F peak representing the decomposition of PF_6^- only existed on the surface of the material, and compared to LRLO (Fig. S33f), its peak is significantly reduced, consistent with the results of the F 1s spectra, and the surface electrolyte decomposition is effectively suppressed.

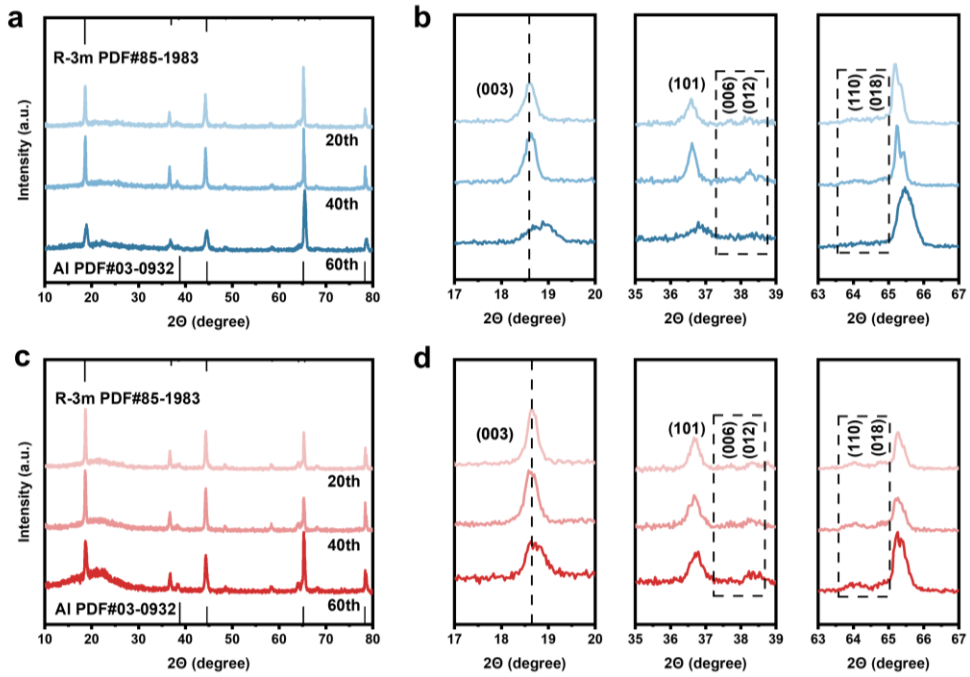

Fig. S34. XRD patterns of (a-b) LRLO and (c-d) LRLO-OG after cycle.

The LRLO and LRLO-OG electrode materials are evaluated and analyzed after cycles. After 60 cycles, the XRD diffraction peak of LRLO (003) migrated markedly to the right, showing c-axis expansion due to interfacial side reactions and structural degradation. A comparison of LRLO and LRLO-OG reveals that the (006)/(012) and (110)/(018) diffraction peaks have significantly merged in LRLO, indicating serious deterioration of the layered structure. In comparison, the splitting of these peaks suggests that the layered structure of LRLO-OG was preserved, implying that the coating layers allow LRLO-OG to maintain its structural stability.

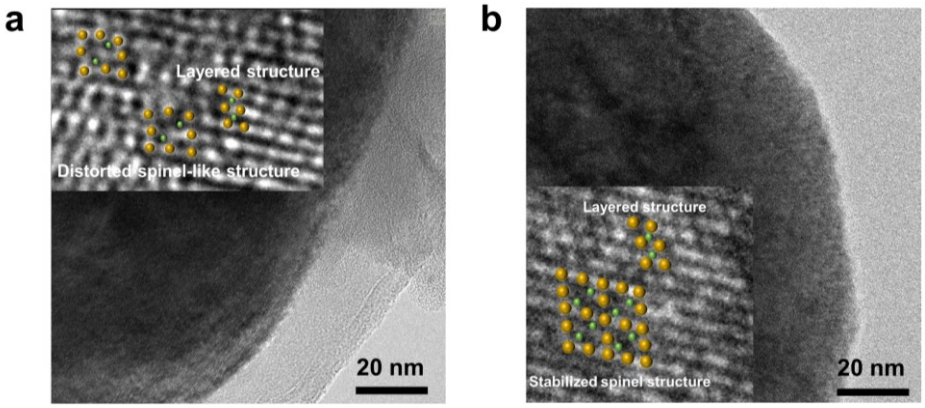

Fig. S35. TEM images of (a) LRLO and (b) LRLO-OG after 20th cycles at 1 C.

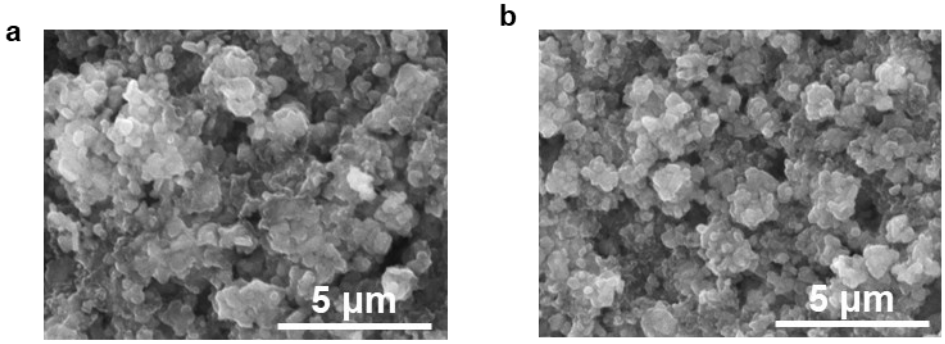

Fig. S36. SEM images of (a) LRLO and (b) LRLO-OG after 20th cycles at 1 C.

References

1. I. Vicente, P. Salagre, Y. Cesteros, F. Guirado, F. Medina and J. Sueiras, *Appl. Clay Sci.*, 2009, **43**, 103-107.
2. B. H. Toby and R. B. Von Dreele, *J. Appl. Crystallogr.*, 2013, **46**, 544-549.
3. J. P. Perdew, K. Burke and Y. Wang, *Phys. Rev. B*, 1996, **54**, 16533-16539.
4. J. P. Perdew, K. Burke and M. Ernzerhof, *Phys. Rev. Lett.*, 1996, **77**, 3865-3868.
5. Z. Qu, Y. Muhammad, W. He, J. Li, Z. Gao, J. Fu, S. Jalil Shah, H. Sun, J. Wang, Z. Huang and Z. Zhao, *Chem. Eng. J.*, 2021, **404**, 126570.
6. S. Grimme, *J. Comput. Chem.*, 2006, **27**, 1787-1799.
7. Y. Wang, Y. Wu, P. Mao, Y. Fan, X. Wang, H. Xiang, Z. Li, K. Li and C. Hu, *Small*, 2023, **20**, 202304898.
8. S. Y. Li, J. P. Ji, Z. H. Li, L. J. Yan, W. Jiang, M. Ling, Z. Lin and C. D. Liang, *Z. Anorg. Allg. Chem.*, 2020, **646**, 1285-1291.
9. X. Ding, D. Luo, J. Cui, H. Xie, Q. Ren and Z. Lin, *Angew. Chem. Int. Ed. Engl.*, 2020, **59**, 7778-7782.
10. B. Qiu, J. Wang, Y. Xia, Z. Wei, S. Han and Z. Liu, *ACS Appl. Mater. Interfaces*, 2014, **6**, 9185-9193.
11. H. Nguyen and R. J. Clément, *ACS Energy Lett.*, 2020, **5**, 3848-3859.
12. J. H. Song, J. H. Shim, A. Kapylou, D. H. Yeon, D. H. Lee, D. H. Kim, J. H. Park and S. H. Kang, *Nano Energy*, 2016, **30**, 717-727.
13. D. Wang, C. Xin, M. Zhang, J. Bai, J. Zheng, R. Kou, J. Y. Peter Ko, A. Huq, G. Zhong, C.-J. Sun, Y. Yang, Z. Chen, Y. Xiao, K. Amine, F. Pan and F. Wang, *Chem. Mater.*, 2019, **31**, 2731-2740.
14. S. H. Yuan, H. Z. Zhang, D. W. Song, Y. Ma, X. X. Shi, C. L. Li and L. Q. Zhang, *Chem. Eng. J.*, 2022, **439**, 135677.
15. S. Burke and J. F. Whitacre, *Adv Sci (Weinh)*, 2023, **10**, 2300068.
16. W. Li, J. A. Quirk, M. Li, W. Xia, L. M. Morgan, W. Yin, M. Zheng, L. C. Gallington, Y. Ren, N. Zhu, G. King, R. Feng, R. Li, J. A. Dawson, T. K. Sham and X. Sun, *Adv. Mater.*, 2023, **36**, 2302647.
17. B. Chen, J. Zhang, T. Wang, T. Li, C. Liu, L. Sun, X. Liu and D. Wong, *Angew. Chem. Int. Ed. Engl.*, 2023, **136**, 202315856.
18. M. Yao, Q. Q. Ruan, Y. Y. Wang, L. Y. Du, Q. G. Li, L. Xu, R. J. Wang and H. T. Zhang, *Adv. Funct. Mater.*, 2023, **33**, 2213702.
19. M. Yao, Q. Q. Ruan, S. S. Pan, H. T. Zhang and S. J. Zhang, *Adv. Energy Mater.*, 2023, **13**, 2203640.
20. R. Yu, C. Wang, H. Duan, M. Jiang, A. Zhang, A. Fraser, J. Zuo, Y. Wu, Y. Sun, Y. Zhao, J. Liang, J. Fu, S. Deng, Z. Ren, G. Li, H. Huang, R. Li, N. Chen, J. Wang, X. Li, C. V. Singh and X. Sun, *Adv. Mater.*, 2023, **35**, 2207234.
21. S. J. Hu, Y. Li, Y. H. Chen, J. M. Peng, T. F. Zhou, W. K. Pang, C. Didier, V. K. Peterson, H. Q. Wang, Q. Y. Li and Z. P. Guo, *Adv. Energy Mater.*, 2019, **9**, 2112088.
22. Z. P. Shi, Q. W. Gu, L. Yun, Z. N. Wei, D. Hu, B. Qiu, G. Z. Chen and Z. P. Liu, *J. Mater. Chem. A*, 2021, **9**, 24426-24437.
23. S. D. Worley, C. H. Dai, J. L. Graham, A. T. Fromhold, K. Daneshvar, A. F. Whitaker and S. A. Little, *J. Spacecr. Rockets*, 1986, **23**, 350-352.
24. D. T. Clark, W. J. Feast, D. Kilcast and W. K. R. Musgrave, *J. Polym. Sci. Polym. Chem. Ed.*, 1973, **11**, 389-411.